Undergraduate Research Project 2
Final Report

Student: Matar Melody Rosen

Report submitted to: Asst. Professor Igal Kronhaus

Advisors:
Asst. Professor Igal Kronhaus
Anton Ronis

Aerospace Plasma Laboratory, Faculty of Aerospace Engineering, Technion

April 2020

Course number: 085852

Contents

List of Figures

List of Tables

Nomenclature

ΔReattachment	Precentile change in reattachment length
$\dot{m}_\infty$	Mass flux
$\langle P_{arc} \rangle$	Average arc power
ρ_∞	Air density
A	Test section area
c_p	Isobaric specific heat
D	Duty cycle
E_{pulse}	Pulse energy
f_{ac}	Actuation frequency
h	Step rise
h_t	Flow enthalpy
I	Current
I_{arc}	Arc current
n	number of pulses in the packet
St_h	Strouhal number based on step height
t	time
T_∞	Ambient temperature
t_{arc}	discharge duration, in which the IGBT is in its 'off' state
t_{charge}	Coil charging duration
T_{cycle}	Actuation cycle time $T_{cycle} = 1/f_{ac}$
t_{on}	Time in which the IGBT is in its 'on' state
$t_{shut-off}$	the time the IGBT takes to shut off
u_∞	Freestream velocity
V	Voltage
V_{arc}	Discharge voltage
V_{IGBT}	IGBT drain source voltage
V_{supp}	Supply voltage
X	distance between the step riser and the reattachment line
L	Length prior to the rise
W	BFS span

Abbreviations

AFC	Active Flow Control
APL	Aerospace Plasma Labratory
BFS	Backward Facing Step
CAA	Cathodic Arc Actuator
CAD	Computer aided design
CAJ	Cathodic Arc Jet
DBD	dialectric-barrier-discharge
IGBT	Insulated-Gate Bipolar Transistor
LAFPA	local arc fillament plasma actuator
PPU	Power Processing Unit

Report Introduction

Scope

This report summarizes the progress made in the recent year: investigations regarding the Cathodic Arc Actuator (CAA) and its Power Processing Unit (PPU). It includes the findings from the subsonic backward facing step reattachment length tests, as well as PPU software and hardware updates for high frequency actuation.

Outline of the Report

The report is divided into chapters as follows:

Chapter 1

The first chapter deals with the investigation of the performance of the CAA as a flow control device in subsonic flow over a backwards facing step (BFS). The planing of the experiment was documented in the previous report [2], the main findings were presented in the 60th Israel Annual Conference on Aerospace Sciences (IACAS) [3]. The chapter includes an abbreviated introduction, the experimental setup, the results (including those too raw to formally publish), and a discussion.

Chapter 2

The second chapter documents preparation for a high frequency experiment: power dissipation analysis, changes to the PPU and to the operating regime. Estimation of the PPU's coil inductance, using current measurements. High flow velocity is characterised with high natural frequencies, thus high actuation frequencies are required for flow excitation. The purpose of this project had been to improve the software and PPU hardware to enhance the efficiency of the circuit in high frequency actuation.

Appendices

The last version of the program is provided in appendix A and the IGBT manufacturer's data sheet is in appendix B.

Chapter 1

The Influence of CAJ on Separated Subsonic Flow Over Backward Facing Step

1.1 Introduction

Flow control devices are usually divided to passive and active categories. Passive devices manipulate the flow by structural means and require no energy to operate, while active flow control (AFC) devices may act on the flow by various means and require energy to operate. AFC methods are further classified as steady and periodic.

Steady means such as blowing and suction of air were shown to improve lift and reduce drag in aerodynamic platforms [4]. Despite these benefits, the implementation of these ideas turned inefficient due to increased weight and complex design requirements that overcame the performance gain.

Periodic control devices aim to excite specific flow instabilities to affect the flow field [4, 5]. These perturbations can be generated by various means. Several examples include: synthetic jets, and non-zero mass flux jets [6]; moving object/surfaces that interact with the local flow field [7]; plasma actuators, characterized by no moving parts, low mass and fast time response [8]. As these type of devices manipulate existing flow instabilities, they usually require less momentum to operate compared with steady devices and are therefore easier to implement [4].

1.1.1 Plasma Actuators

Plasma actuators are active periodic devices that act on the flow by the usage of an electrical discharge. Low power devices associated with corona, and glow discharges such as the dialectric-barrier-discharge (DBD) [8] are very common and are applied for the manipulation of low speed flow regimes. High power devices are associated with arc discharge and are usually based on surface plasmas, local arc fillament plasma actuator (LAFPA) [9]- for example. When active, plasma actuators introduce a plume of fast ions from electrode material that collide with flow particles thus inserting momentum into the flow (non-thermal plasma) or local heating of the flow (thermal plasma). Thermal plasma actuators, excite the flow by localized heating that creates pressure perturbations [10]. Non-thermal plasma actuators excite the flow using discharge-induced electric wind [8], usually with flush mounted electrodes that accelerate the flow tangential to the wall.

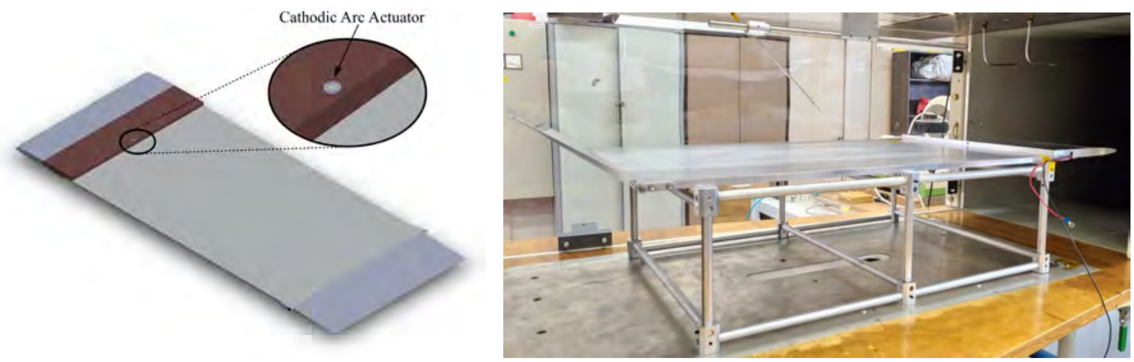

Figure 1.1: CAD drawing (left) and photograph (right) of the BFS model. The right image is the model inside the test section, the flow is from right to left, Pitot tubes and a hot wire probe can be seen as well.

1.1.2 Cathodic Arc Jet

An electric arc is an electrical discharge between two electrodes, characterized by high current and low voltage. A cathodic arc is a type of electric arc that is maintained through the production of highly ionized plasma by a combination of joule heating and ion bombardment heating that maintain the conditions required for electron emission and vaporization of cathode material. When generated in vacuum cathodic arcs produce fast plasma plumes. Cathodic arcs in atmospheric pressure gas produce fast jets of gas, termed cathodic arc jets (CAJ) [11]. The cathodic arc actuator (CAA) is a device that generates CAJs, developed in the Aerospace Plasma Laboratory (APL) in the Technion.

1.2 Experimental Setup

The experiment was conducted at the Aerospace Faculty Subsonic Wind Tunnel 15, Technion: a closed loop tunnel with test section dimensions of: $0.5\ m \times 0.5\ m \times 1.37\ m$. The wind tunnel velocity was measured with two pitot tubes placed parallel to the flow at the beginning of the test section, producing dynamic pressures, translated into a voltage reading by a MKS BARATRON 398HD pressure transducer, from which the velocity is calculated. The aerodynamic test bed for the experiment is presented in Fig. 1.1, the left image is the computer aided design (CAD) and the right image is of the model inside the test section, the flow is from right to left. In the right image, Pitot tubes used to calibrate the wind tunnel velocity can be seen in the upper right corner, and a hot wire probe appears at the top-center of the image. The model dimensions: rise of $h = 10$ mm, span of $W = 450$ mm, and length prior to the rise of $L = 150$ mm, comprised from a half ellipse leading edge, and a straight section before the edge (75 mm,75 mm).

1.2.1 Actuator and Electric Setup

The actuator used in the experiments can be seen in Fig. 1.2. It is composed of an inner tungsten anode 0.8 mm in diameter, external 7 mm stainless steel cathode, and an alumina insulator diameter of 2.5 mm. The cathode is threaded and screwed into the model. The CAA is powered by an inductive power processing unit (PPU) that includes a 1.7 kV insulated-gate bipolar transistor (IGBT) connected between the anod and common ground. When the IGBT is "on", the coil is charged by the passing current. When the IGBT is switched "off", the sudden change in the circuit creates a high voltage spike between the electrodes, igniting the arc while high current passes from the coil through the arc [12]. The circuit logic is governed by an on-board microprocessor (or with a signal generator). In the following experiments, two types of PPUs were used: the first version (shown schematically in Fig.1.3) had a single switch and was used for the long pulse operation and for the pulse train; The second PPU had an additional IGBT controlling the discharge duration,

Figure 1.2: Visible photograph of the CAA used for the experiment. The anode, cathode and insulator are labeled.

which was used to produce a single short pulse. Fig. 1.3 schematically presents the electrical setup with the first type of PPU. The circuit was probed by a Pearson coil (model 150), for discharge current measurement, and a 100:1 high voltage probe for measurement of discharge voltage. Both current and voltage signals were recorded on a 5 GS/s digital oscilloscope.

1.2.2 Flow Diagnostics

Oil Flow Visualisation

A Silicon oil was spread at the vicinity of the actuator, to illustrate the reattachment line. A CMOS camera placed on top of the test section was used to make a video recording of the oil structure. The video was then post-processed to yield the reattachment length of the recirculation region.

Hot Wire anemometry

The normal velocity near the model was measured by a hot wire anemometry system of A. A. Lab Systems. The hot wire measurement device includes a probe (DANTEC, type 55P11, straight prongs, with the sensor perpendicular to probe axis), and a $5\mu m$ diameter tungsten sensor (900 Ω/ft). The hot wire was kept at an overheat ratio of 1.6, where it has a maximum frequency response of 30 KHz (according to the manufacturer). The hot wire was calibrated by recording its voltage reading when placed near the wind tunnels velocity probes, and running the wind tunnel at a range of known velocities. A fitting curve had been applied to the voltage-velocity recordings.

The probe was mounted on a three-axis traversing mechanism, with resolution of 5 μm in the vertical direction, and 1 mm in streamwise and spanwise directions. We used a LabVIEW software to automatically control the location, and measurement time of the probe in different stations, this way we were able to measure boundary layer velocity profiles at different positions over the model.

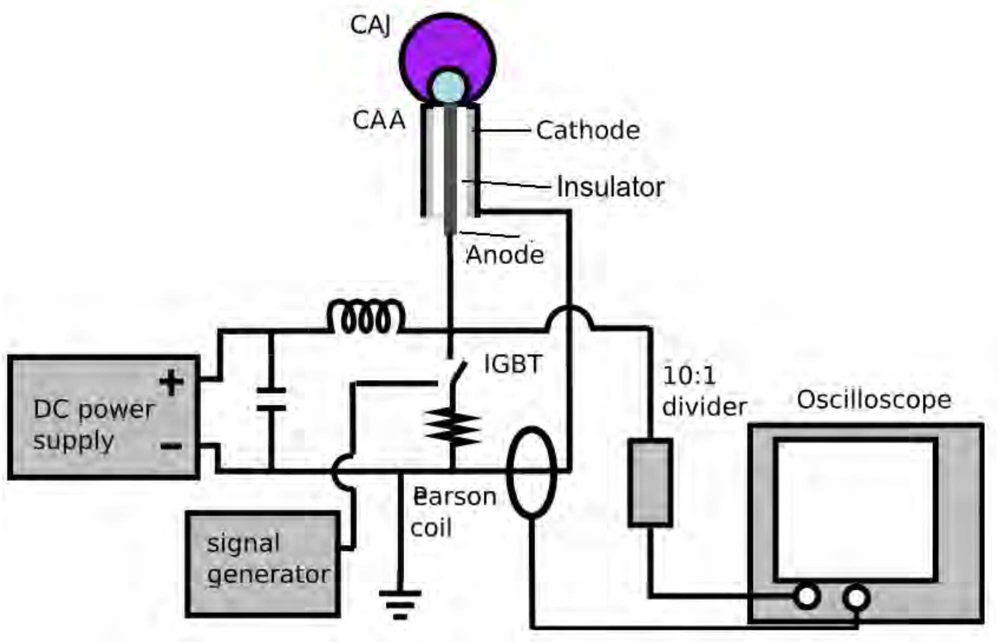

Figure 1.3: Schematics of the CAA, the power processing unit and electrical measurement setup.

1.3 Results and Discussion

1.3.1 Electric Measurements

This section presents the electric performance of the actuator in the different modes of operation while operating inside the wind tunnel. Figures 1.4 – 1.7 depict the voltage and current time histories for several modes of operation. They are characterized by the following parameters:

- Pulse duration.
- Peak current I_{arc}.
- Supply voltage V_{supp}.
- Arc voltage, assumed to be constant: $V_{arc} = 30\ V$.
- Charging duration – the time duration used to charge the coil before discharge.
- Duty cycle D.
- Pulse energy $E_{pulse} = \int_0^{tf} IV\mathrm{d}t$

These parameters are calculated for each mode of operation and are presented in Table 1.1.

Fig. 1.4 presents the reference mode of operation: uncut pulse duration, single pulse, $V_{supp} = 20\ V$.

Long pulse duration, and high supply voltage IV curve is presented in Fig. 1.5.

A single short pulse was generated using the PPU with two switches, and supply voltage of $V_{supp} = 35\ V$, the IV curve is presented in fig. 1.6. This type of operation had been shown to produce the largest thrust and thrust to power ratio in quiescent air [12].

Fig. 1.7 presents an example of the pulse modulated case – a three pulse train, in which the first two pulses are cut ($\sim 5\ \mu s$) and the third is uncut and lasts for the rest of the discharge (completing to a total discharge duration of $\sim 50\ \mu s$). This mode of operation was preformed with the single switch PPU.

Case #	Pulse duration μs	Peak arc current A	Supply voltage V	Charging time μs	Duty cycle %	Pulse energy mJ
1.3.2	45	40	20	200	0.125–0.875	30
1.3.2	140	60	35	200	0.25	108
1.3.2	5	55	35	100	0.025	8.25
1.3.2	50	40	20	200	0.2	33

Table 1.1: Calculated pulse parameters.

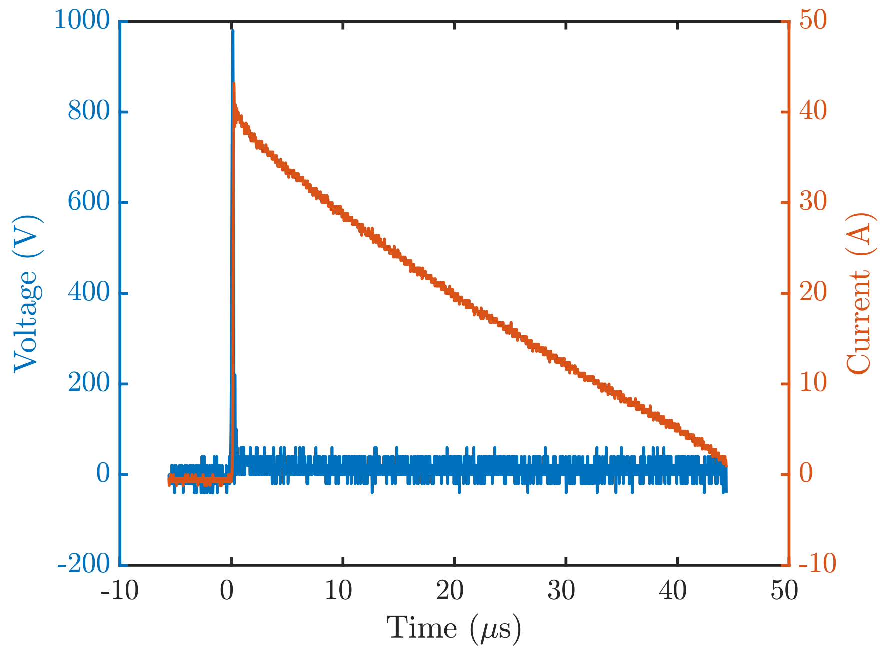

Figure 1.4: Long pulse operation IV curve, V_{supp}=20 V, charging duration 200 μs.

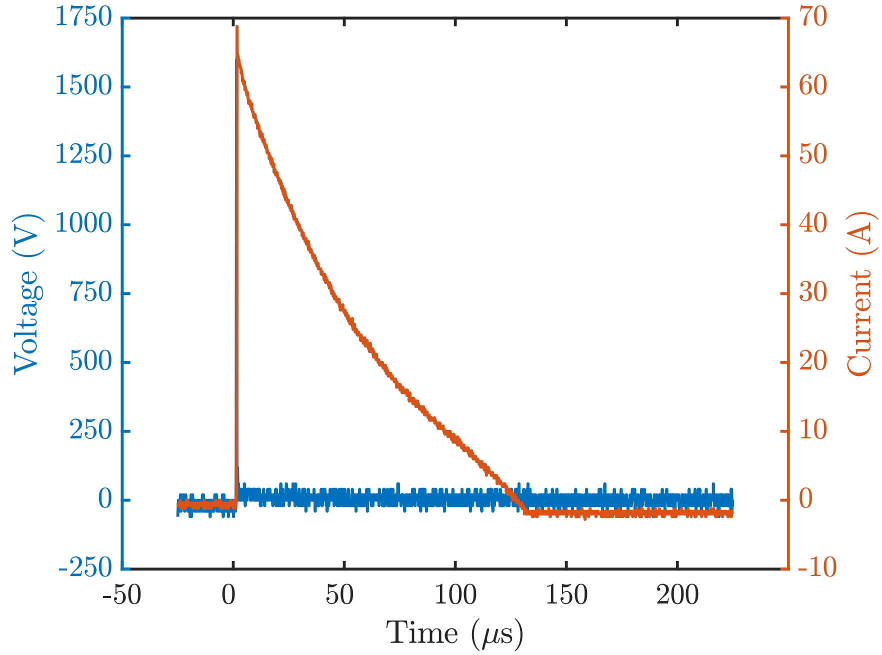

Figure 1.5: Long pulse operation IV curve, high supply voltage: $V_{supp} = 35\ V$, charging duration 200 μs.

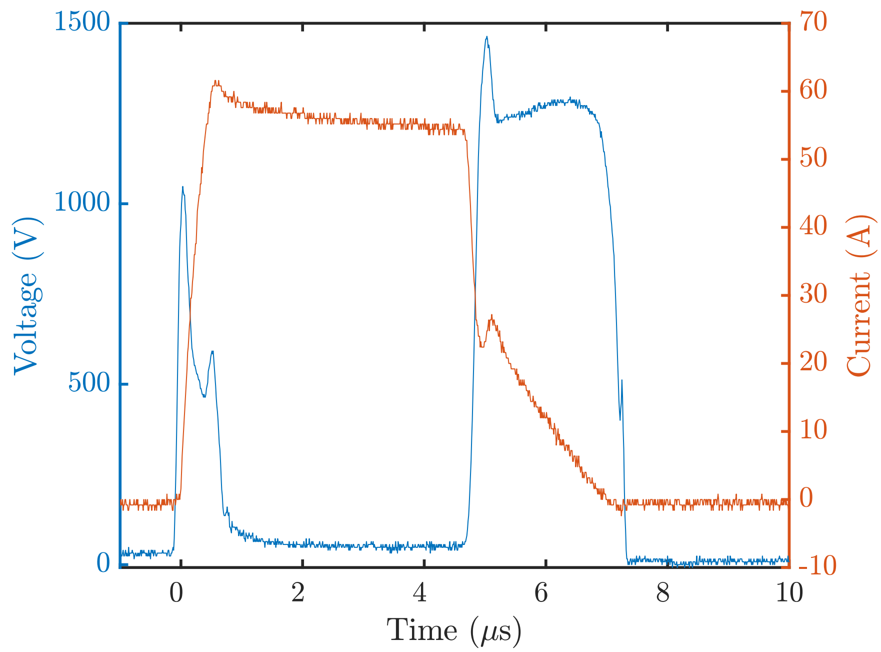

Figure 1.6: Short pulse duration IV curve, $V_{supp} = 35\ V$, charging duration 100 μs.

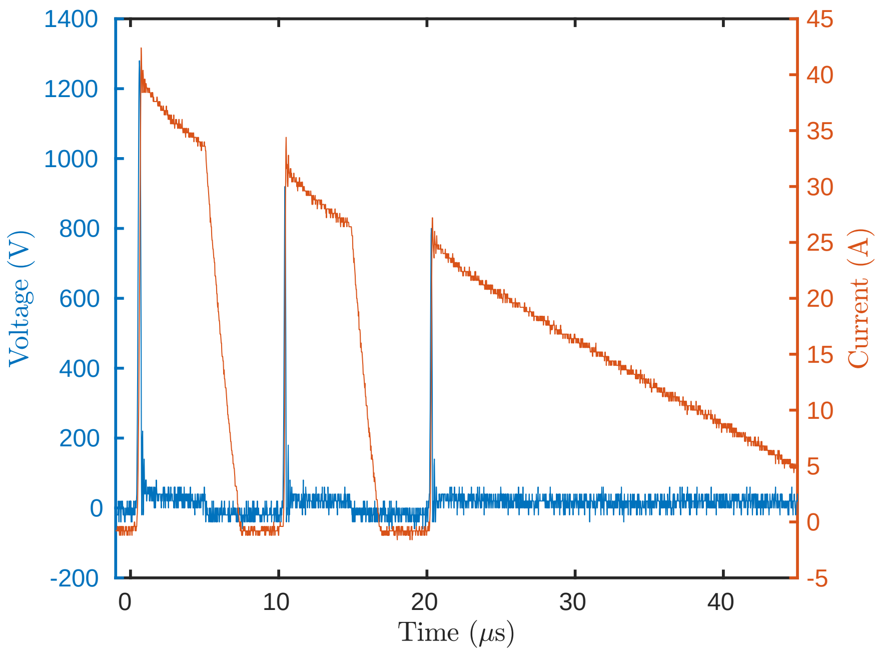

Figure 1.7: Pulse train of three pulses IV curve, $V_{supp} = 20\ V$, charging duration 200 μs.

Figure 1.8: Isometric view of the oil blob deformation on the model. Actuation at 50 Hz, freestream velocity 10 m/s. The reattachment line can be seen.

1.3.2 Oil Flow Visualisation

The reattachment is seen through the boundary between the oil and model surfaces, see fig. 1.8 for a visible photograph of the oil blob boundary deformation due to the CAA operation. As the flow in the wind tunnel stabilizes, the oil puddle was gathered and shaped by the separation bubble that developed near the step. When actuated, the border of the oil blob deformed which visualizes the effect the actuator has on the reattachment line.

The difference between baseline and actuated reattachment lines was then calculated to produce the effect of the CAA on the recirculation region. Fig. 1.9 depicts the process by which the oil visualisation results were processed: By taking the coordinates of the step riser, and the closest point of oil boundary, the reattachment distance with respect to the step had been calculated, both in the actuated and unactuated (baseline) cases. This has been done by hand and performed several times to quantify the error of measurement and to reduce uncertainty.

Long Pulse Duration

The change in reattachment length for different actuation frequencies was measured with the actuator placed perpendicular to the flow. The frequencies were in the range of $f_{ac} \in 25 - 175Hz$, translating to Strouhal numbers range of $St_h \in 0.025 - 0.175$.

Fig. 1.10 presents schematic depiction of the reattachment length for both baseline and actuated operation for the different tested frequencies. Each figure shows a top view scheme of the model, the horizontal axis describes the distance from the step (black dashed lines), in the freestream direction, normalized by step height (X/h). The baseline reattachment line in each figure is represented by green dashed lines and is located at $X/h \sim 4$. The actuated reattachment line for each frequency is represented by blue dashed lines, located in the range of $2.85 < x/h < 3.7$. The uncertainty in the distance measurements (colored area) were estimated by repeating each measurements several times. From the results presented in Fig. 1.10 it can be observed that in all tested frequencies the reattachment length shortened, with the most significant improvement obtained at a frequency of 125 Hz. Since the flow parameters stay constant, we can expect that the unactuated reattachment line would be constant, and despite the uncertainties, it is quite unchanging, unlike the actuated case that appears to vary with the change of actuation frequency.

Fig. 1.11 shows the percentile change in reattachment length of the actuated case compared to the

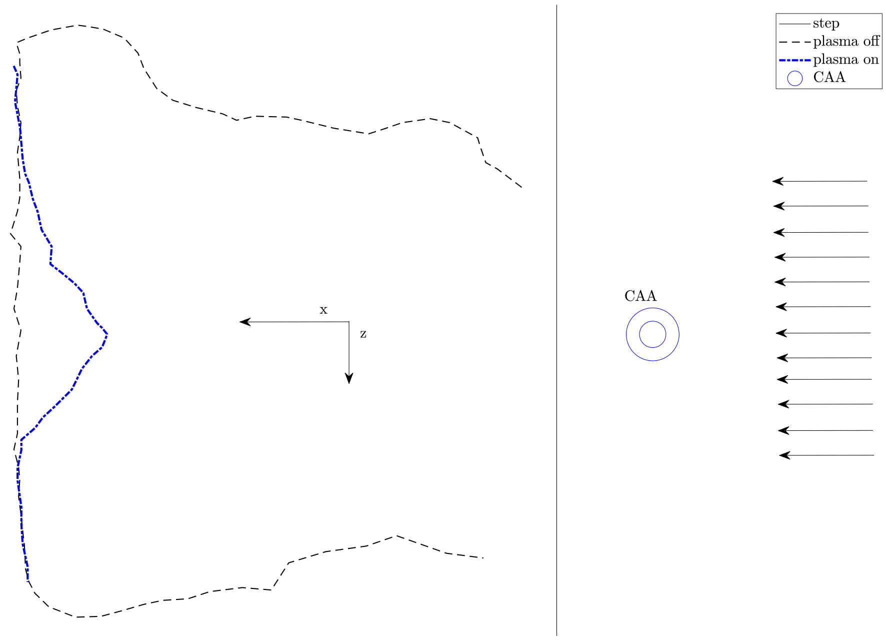

Figure 1.9: Top view schematics of the oil puddle on the model, actuated reattachment line (dashed-dot blue) and base reattachment line (dashed black). Step riser, actuator location and direction of the flow indicated. Actuation frequency: 50 Hz, freestream velocity: 10 m/s.

baseline for different actuation frequencies. In addition, the change in reattachment to normalized power ratio is presented versus frequency of actuation, normalized by the maximum value. These were calculated in the following manner:

$$\Delta X = \frac{X_{unactuated} - X_{actuated}}{X_{actuated}}, \tag{1.1}$$

where X denotes the distance between the step riser and the reattachment line, for the actuated and unactuated cases. ΔReattachment is the percentile of ΔX. The normalized power was calculated from:

$$\overline{P} = \frac{\langle P_{arc} \rangle}{\dot{m}_\infty h_t} = \frac{\langle I_{arc} V_{arc} \rangle}{\rho_\infty A u_\infty (c_p T_\infty + u_\infty^2)} \tag{1.2}$$

where $\langle P_{arc} \rangle$ is the average arc power, in which I_{arc} is the discharge current and V_{arc} is the discharge voltage. $\dot{m}_\infty$ is the mass flux over the model, h_t is the flow enthalpy, ρ_∞ air density, A is the area of the test section, u_∞ is the freestream velocity, c_p is the isobaric specific heat, and T_∞ is the ambient temperature.

The normalized change in reattachment changes linearly with frequency up to $\sim$ 125 Hz where it reaches a maximum at $\sim$ 35 %. It then drops to $\sim$ 20 %. As the average power is proportional to the frequency, and the change in reattachment rises almost linearly with the frequency, the resultant energetic efficiency is nearly constant for frequencies lower than $f_{ac} = 125$ Hz. Higher frequencies require more energy have lower change in reattachment and are therefore less energetically favourable.

Long pulse duration - Parallel orientation

The next set of experiments were done in order to compare the effects of the actuator when placed in different orientation. The mechanism in which the actuator interacts with the flow depends on it's position relative to the flow, while perpendicular, the actuator periodically blocks the flow thus generating some 3d instabilities.

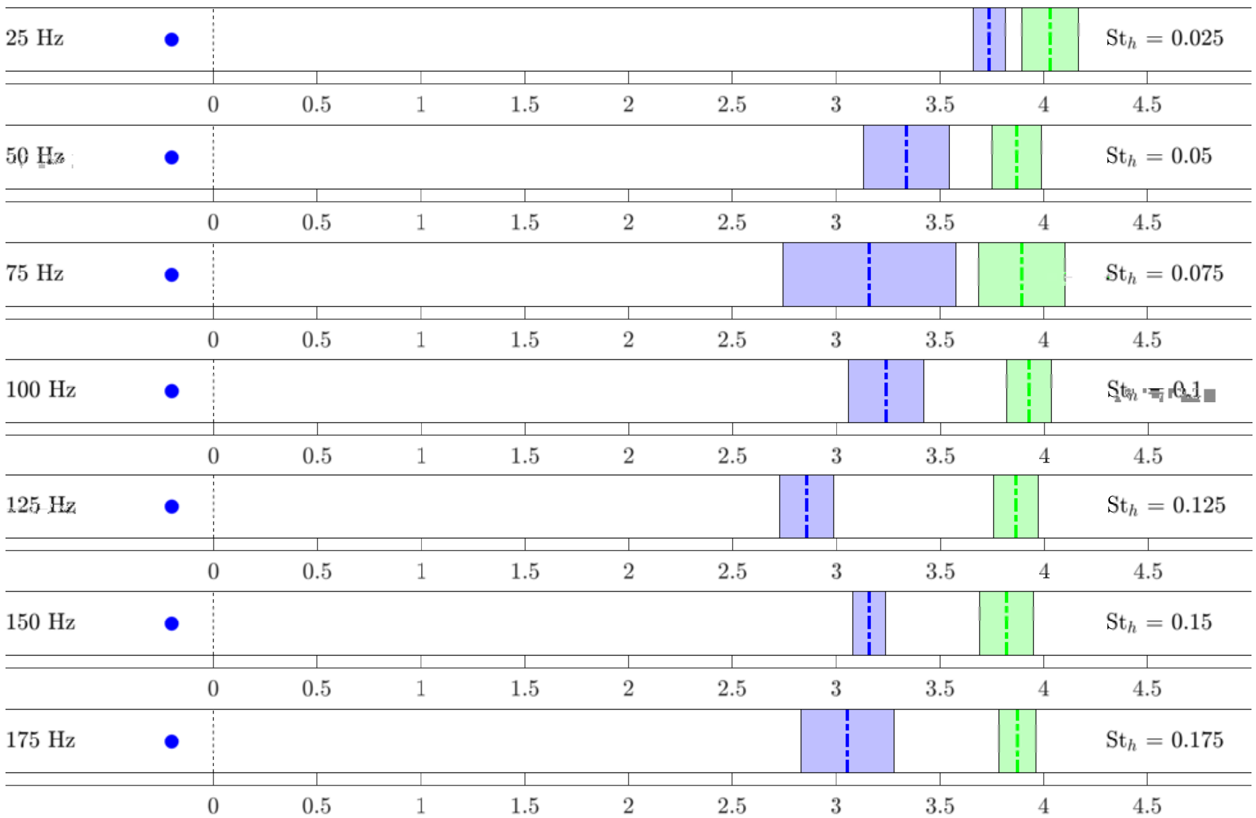

Figure 1.10: Schematic top view of the model, with indications of the actuator location (blue dot), step riser (dashed black), base reattachment line (green dashed), actuated reattachment line (blue dashed) and uncertainties (colored area). Actuation frequency, strouhal number and distance from the step rise (normalized by step height) are also indicated. Freestream velocity was 10 m/s, and the actuator was in perpendicular position.

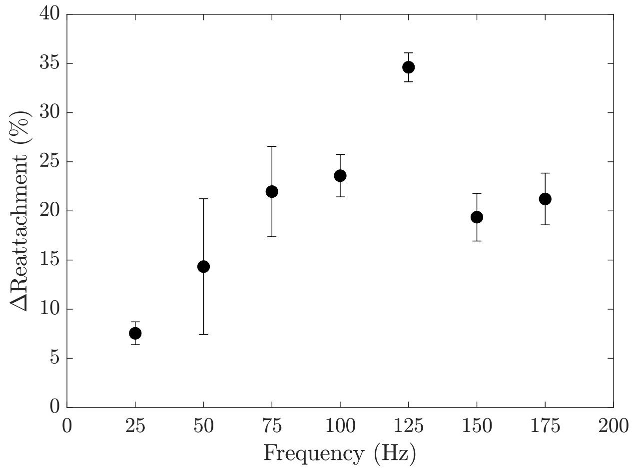

(a) Difference in reattachment vs. actuation frequency.

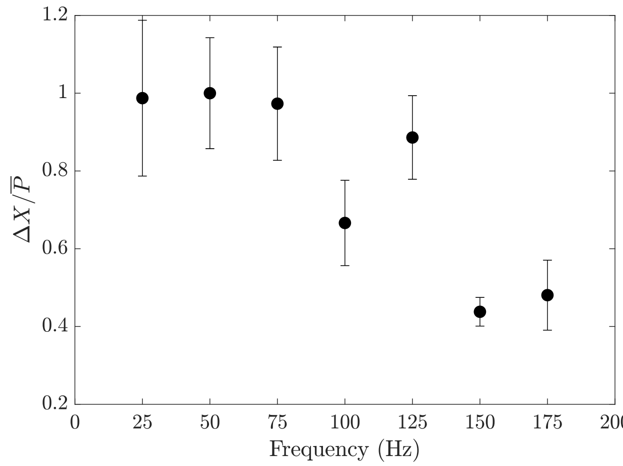

(b) Ratio between reattachment line difference and average arc power vs. actuation frequency.

Figure 1.11

When the jet is parallel, the mechanism might be different, perhaps due to momentum transfer but more likely due to thermal effects, similar to LAFPA [10] and other thermal plasma actuators. Fig. 1.12 presents the results of parallel actuation in several frequencies. As before, a clear effect on the reattachment line can be observed.

The same post-processing procedure was performed to produce Fig. 1.13. Unlike the perpendicular orientation, no clear trend versus frequency is observed for the change in reattachment for the parallel actuation. However, a notable advantage can be observed for actuation in the lowest frequency range. This difference suggest that the CAA orientation changes the mechanism of influence of the CAA on the flow.

High pulse energy

The oil deformation obtained for higher pulse energy is presented schematically in Fig. 1.14.

Unlike the lower pulse energy, the deformed boundary doesn't show a favourable decrement in reattachment length at the centerline. Moving away from the centerline in the spanwise direction shows a reduction of reattachment length. This suggests the existence of a complex 3D effect when operated with high pulse energies. This effect may be attributed to the larger geometrical plume size acting as a virtual fence to the flow.

Single Short Pulse Duration

The two switches PPU had been used to generate a pulse with short discharge duration ($\approx 5\ \mu s$). The effect of this type of discharge on the reattachment distance had been tested in perpendicular orientation, actuation frequency of $f_{ac} = 50\ Hz$ and supply voltage of $V_{supp} = 35\ V$. It was found that the short pulse had greater effect on the reattachment length as seen in Fig. 1.15 compared to the single long pulse duration. In addition to the improved performance, the short pulse requires less energy than the longer pulse leading to a greater efficiency. This supports previous studies that reported higher absolute thrust and efficiency of the CAA when operated with short pulses [12].

These results are summarized in Table 1.2: From these results it can be concluded that short pulse duration is an optimal operation regime for reduction of the reattachment line.

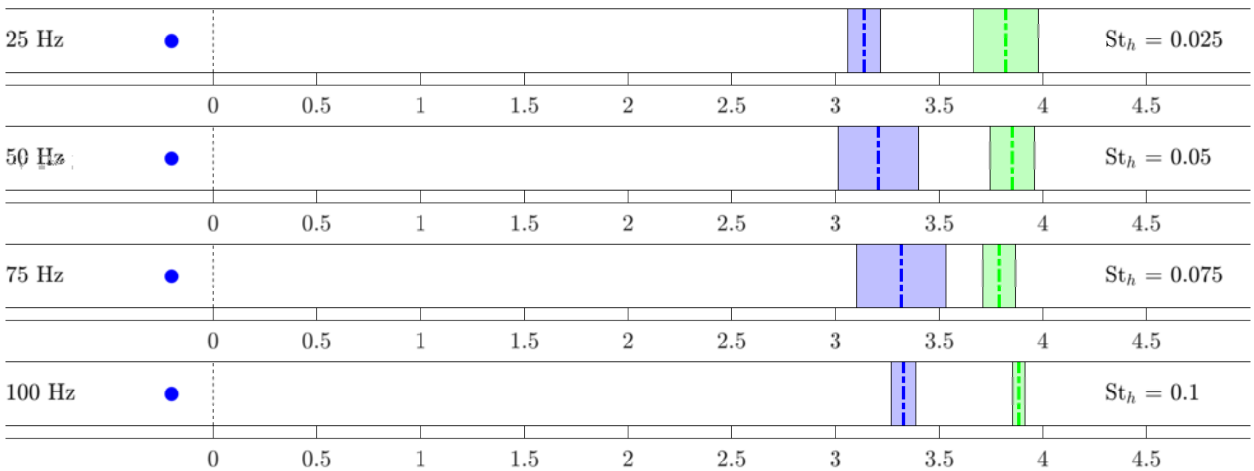

Figure 1.12: Schematic top view of the model, with indications of the actuator location (blue dot), step riser (dashed black), base reattachment line (green dashed), actuated reattachment line (blue dashed) and uncertainties (colored area). Frequency, strouhal number and distance from the step rise (normalized by step height) are also indicated. Freestream velocity was 10 m/s, and the actuator was in parallel position.

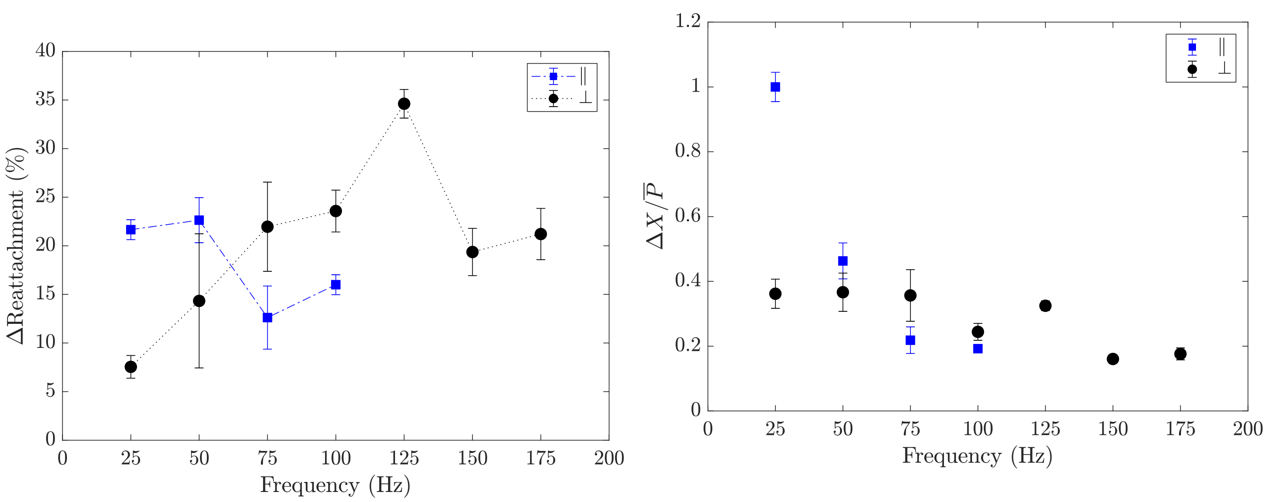

(a) Difference in reattachment vs. actuation frequency.

(b) Ratio between reattachment line difference and average arc power vs. actuation frequency.

Figure 1.13: A comparison between parallel and perpendicular orientations.

Pulse duration μs	Supply voltage V_{supp}	Δ Reattachment %	Pulse energy mJ
45	20	15	30
5	35	30	8.25

Table 1.2: Compression between long and short pulse duration.

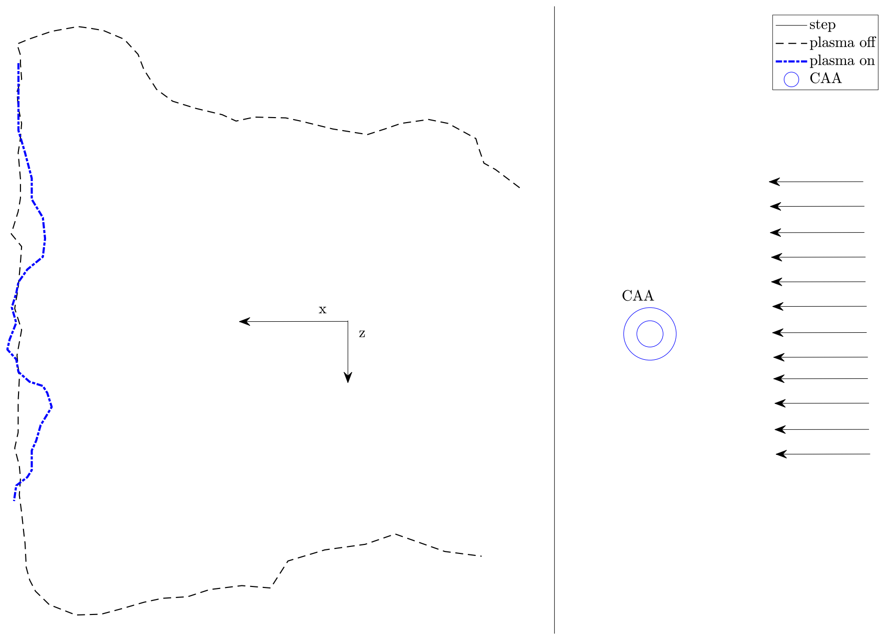

Figure 1.14: Actuation in perpendicular orientation with supply voltage of $V_{supp} = 35\ V$, at $f_{ac} = 50\ Hz$, flow velocity: $10\ m/s$

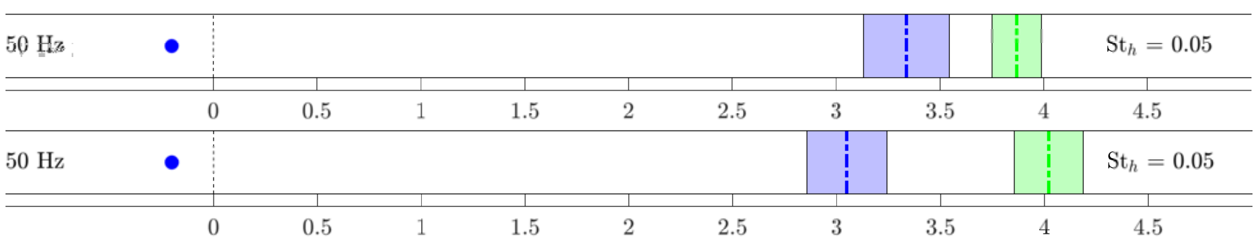

Figure 1.15: Comparison between actuation with long discharge duration (top image, duration: $\sim 45\ \mu s$, supply voltage: $V_{supp} = 20\ V$) and short duration (bottom image, duration: $\sim 5\ \mu s$, supply voltage: $V_{supp} = 35\ V$). Actuation frequency of $f_{ac} = 50\ Hz$ and freestream velocity of: $10\ m/s$.

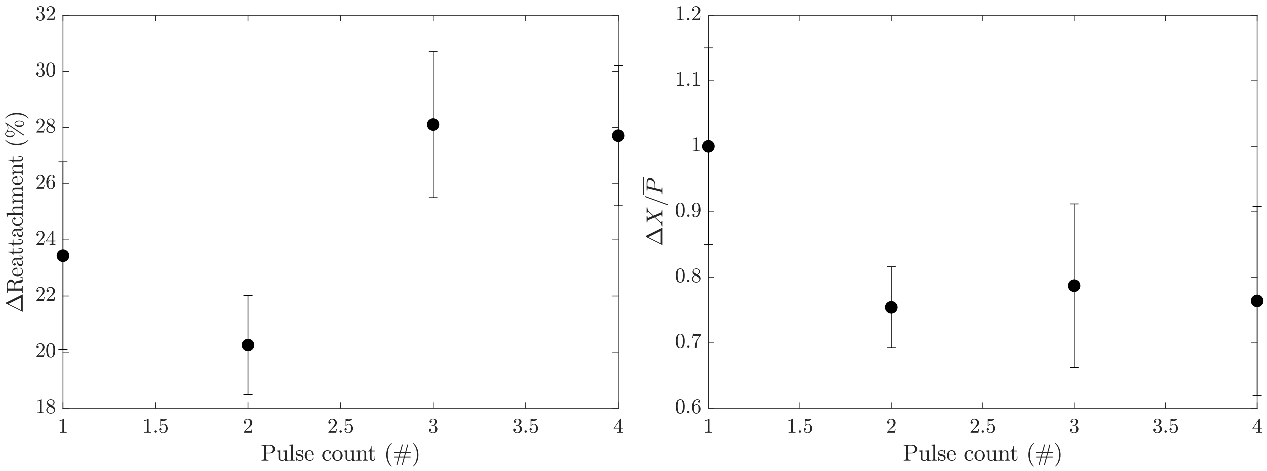

(a) Difference in reattachment vs. number of pulses per packet.

(b) Ratio between reattachment line difference and average arc power vs. number of pulses per packet.

Figure 1.16

Pulse Modulated

A pulse train mode of operation of the CAA was accomplished by using the single switch PPU, actuating at $f_{ac} = 50\ Hz, V_{supp} = 20\ V$ and changing the number of pulses per packet. The total discharge duration in each packet is 50 μs, and it consists of several pulses cut at 5 μs and a final uncut pulse lasting until the exhaustion of the coil.

Fig.1.16 compares the reattachment reduction and normalized energetic efficiency of a pulse train versus several pulse numbers per packet. Despite increasing the number of pulses per packet, no clear improvement of reattachment reduction was observed. This could possibly be explained by the short recovery time (= 5 μs) applied between adjacent pulses, in comparison to the local flow time scale (10 m/s $\Big/$ 2.5 mm $\approx$ 250 μs). This causes the flow to be affected mainly by the total pulse duration and to stay indifferent to the number of pulses per packet.

1.3.3 Hot Wire Results

Fig. 1.17 shows the difference between the actuated and baseline velocity fields (top: actuation in 50 Hz, bottom: actuation in 100 Hz). The red region in the upper part of the rectangle implies that the actuated flow reaches faster velocities at lower height, i.e. the velocity profile recovers faster, the separation bubble height is lower with actuation compared to without actuation. Both actuation frequencies produced larger velocity magnitudes inside the recirculation region in comparison to the baseline, with a slight preference to the actuation frequency of $f_{ac} = 100\ Hz$.

These notions can be inferred from Fig. 1.18 as well: The velocity profiles for unactuated, actuated at $f_{ac} = 50\ Hz$ and at $f_{ac} = 100\ Hz$ (top to bottom accordingly), for several streamwise locations in the region of interest demonstrate that the actuated flow recovers faster. In addition, all streamwise location for the actuated cases showed fuller velocity profile compared to the baseline flow field.

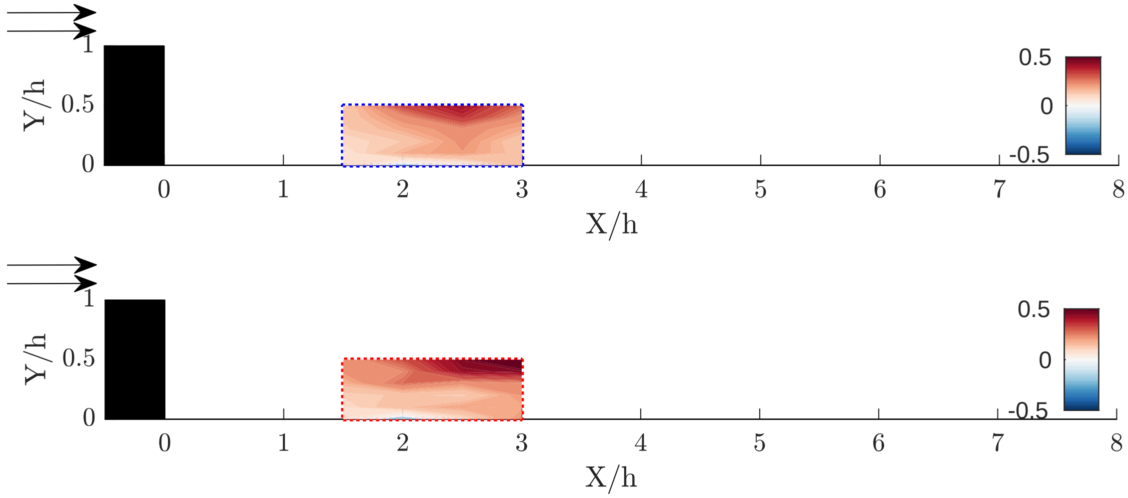

Figure 1.17: Difference in velocity fields between actuated (top- $f_{ac} = 50\ Hz$, bottom- $f_{ac} = 100\ Hz$) and unactuated flow. Velocity units are m/s.

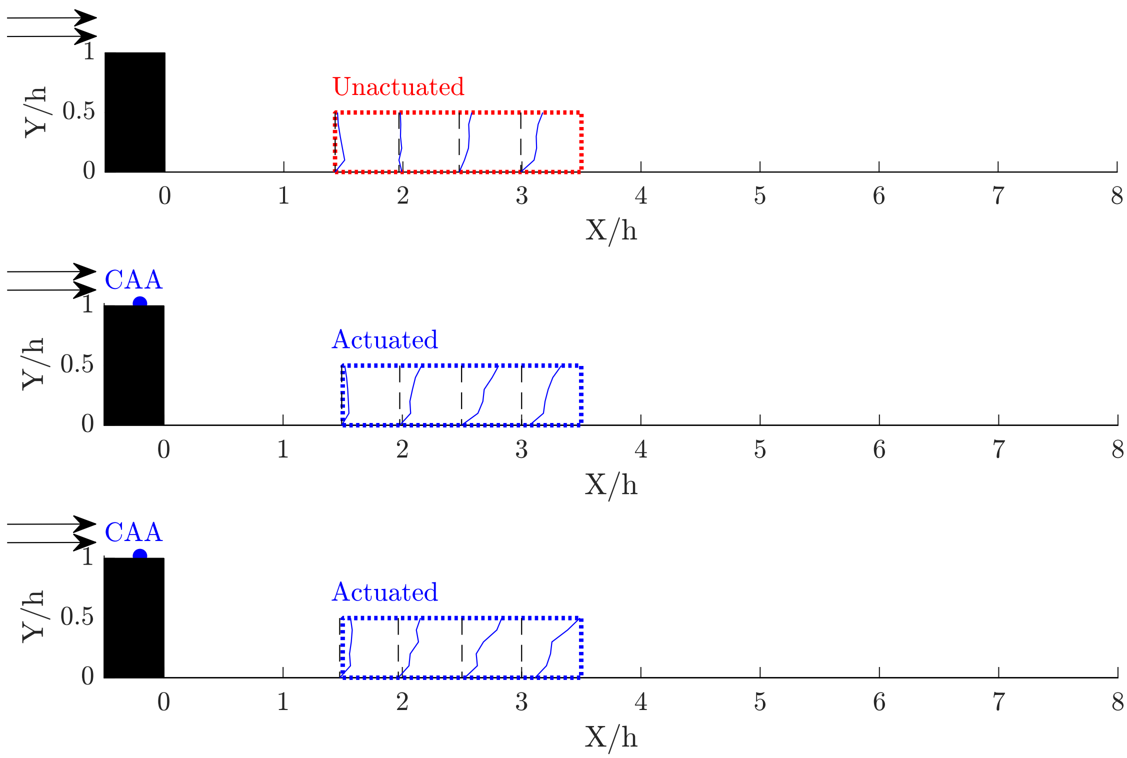

Figure 1.18: Velocity profiles for unactuated, actuated at $f_{ac} = 50\ Hz$ and at $f_{ac} = 100\ Hz$ (top to bottom accordingly), for several streamwise locations.

1.4 Conclusions

The effects of the CAA on subsonic flow reattachment after a backward facing step were investigated experimentally. The CAA was shown to reduce the reattachment length considerably for a wide frequency range of operation. A sensitivity analysis of the CAA parameters on the reattachment length was performed, where the tested variables were: actuation frequency, orientation, pulse duration, pulse energy, and pulse modulation.

The orientation of the CAA effected the reduction in reattachment differently for the tested frequencies of actuation. This suggest that the orientation effects the mechanism of influence of the CAA on the flow.

Higher pulse energies did not seem to improve the reattachment length reduction compared to smaller pulse energies, but seemed to behave as a virtual fence. Possible mechanisms through which the CAJ interacts with the flow and excite flow instabilities had been suggested: periodic momentum addition, pressure and localized heating perturbations, and virtual fencing. Increasing the pulse numbers per packet while keeping the frequency and total pulse duration fixed did not show a clear trend of improvement in the reduction of reattachment length. This was attributed to the considerably smaller delay time between adjacent pulses compared to the flow time scale of recovery.

The best reduction in reattachment was achieved with the short pulse mode of operation. This mode required considerably less energy and therefore resulted in better efficiency. These support previous findings in which the CAA was measured to produce the best thrust and thrust to power ratios for short pulses. The pulse modulated actuation raised the question of flow recovery time- how does the waiting time between pulses influence the flow, and what are the relevant time scales, since the time scales tested here seem to be too short.

Hot wire measurements qualitatively showed a reduction of recirculation region for actuated operation compared to baseline. All together, these findings show that the CAA has a considerable positive effect on the separation region of a BFS subjected to subsonic flow. Future studies will focus on quantitative measurements of the minimal delay time between adjacent pulses in pulse train mode of operation, and on actuation at higher flow velocities.

Chapter 2

Adapting the CAA for High Frequency

2.1 Introduction

The components of interest in the CAA and PPU setup are presented schematically in Fig. 2.1.

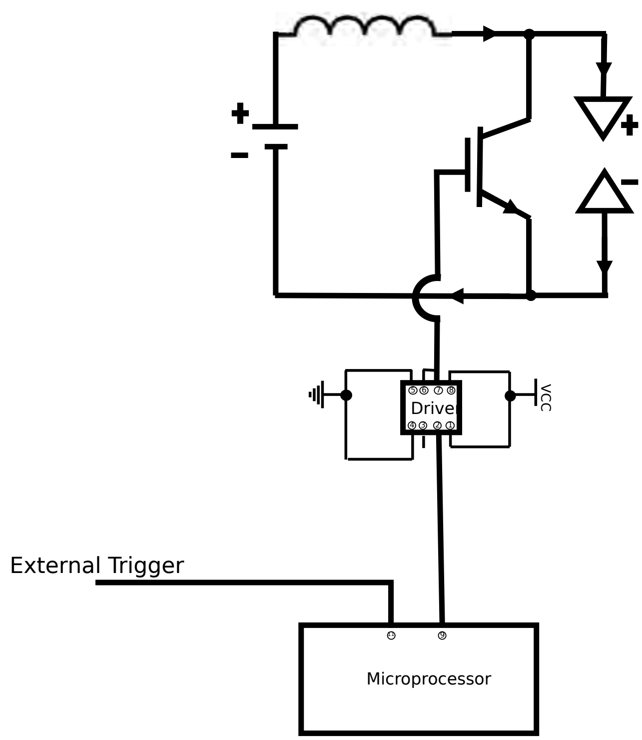

Figure 2.1: Schematic of the PPU

These components are: a DC power supply[1] that charges the inductor. The inductor, used for energy storage, is an air core coil. An Insulated-Gate Bipolar Transistor[2] (IGBT) used to switch between charging

[1]Model: TDK-Lambda GSP100-100
[2]Model: IXGH24N170

and discharging the inductor (leading to a high voltage drop over the CAA electrodes thus igniting the arc). The IGBT is controlled by an Arduino Nano microprocessor (with its own power supply). A driver[3] is used to to convert from the Arduino output voltage (5 V) to the required gate-emitter voltage of the IGBT (15 V).

2.1.1 IGBT and Arduino Nano Specifications

Voltage - Collector Emitter Breakdown (Max)	1700V
Vce(on) (Max) @ Vge, Ic	3.3V @ 15V, 24A
Power - Max	250W
Switching Energy	8mJ (off)
Td (on/off) @ 25°C	42ns/200ns
Test Condition	1360V, 50A, 5Ohm, 15V
Operating Temperature	$-55°C \sim 150°C$ (TJ)

Table 2.1: IGBT IXGH24N170 data from the manufacturer's website [1]

Microcontroller	ATmega328
Architecture	AVR
Operating Voltage	5 V
Flash Memory	32 KB of which 2 KB used by bootloader
SRAM	2 KB
Clock Speed	16 MHz
Analog IN Pins	8
EEPROM	1 KB
DC Current per I/O Pins	40 mA (I/O Pins)
Input Voltage	7-12 V
Digital I/O Pins	22 (6 of which are PWM)
PWM Output	6
Power Consumption	19 mA
PCB Size	18 x 45 mm
Weight	7 g
Product Code	A000005

Table 2.2: Arduino Nano technical specifications

[3] Model: MIC4452YN

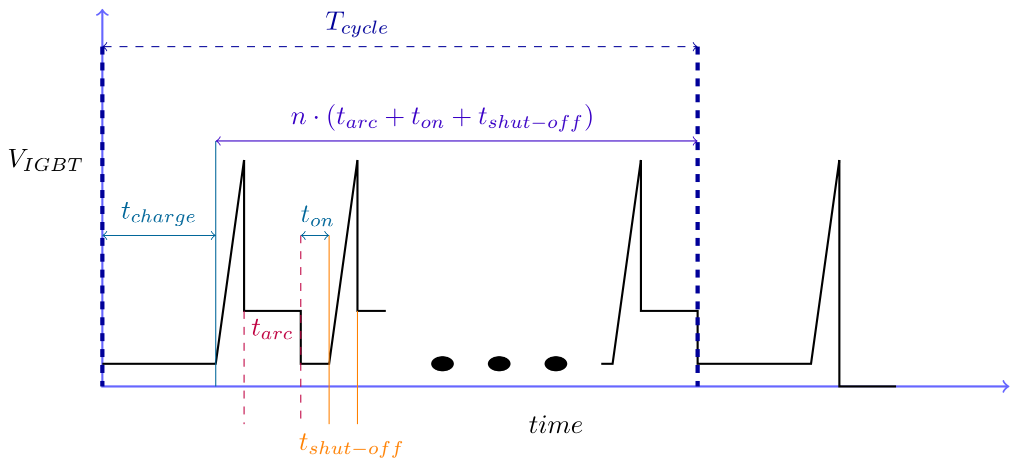

Figure 2.2: Schematics of IGBT voltage in general operation

2.1.2 Objective

Modify the system to comply with the following requirements:

- Actuation frequency 5 KH_z (eventually it was 4 KH_z)
- Short peaked pulses
- Single IGBT circuit, observing the 150 $Watt$ rating of the device
- Control software enhancements:
  - Add 1 s delay before beginning to search for trigger
  - Add some more delay after trigger and before activating

The CAA is most effective and efficient when the arc lasts $\sim 5\ \mu s$ [12], therefore we need to create a short pulse, using the single IGBT circuit (another requirement).

Furthermore, it is explained that during its 'off' time and while turning on, power dissipation on the IGBT has a negligible contribution to its heating.

The implemented solution to the problem: Reduction of coil inductance- to allow faster decay of the arc, and change of the code controlling the PPU to produce the desired operation regime: short peaked pulse at high frequency without overheating the IGBT.

A schematics of the current through the IGBT in a general mode of operation is shown in Fig.2.2. V_{IGBT} is the voltage drop over the IGBT, T_{cycle} is the actuation cycle time ($T_{cycle} = 1/f_{ac}$), t_{charge} is the coil charging duration, in which the IGBT is turned on, t_{on} is again time in which the IGBT is in its 'on' state. n is the number of pulses in the packet, t_{arc} is the discharge duration, in which the IGBT is in its 'off' state and $t_{shut-off}$ is the time the IGBT takes to shut off, which is approximately 0.5 μs [1, 13].

2.2 Experimental Setup

Several current measurement experiments were preformed on the PPU and CAA system described in the introduction. The discharge current was measured with a Pearson coil (model 150) and recorded in a 5 GS/s digital oscilloscope. A signal generator was used as the external trigger for the controller.

Part of the experimental setup is pictured in Fig. 2.3, with several components marked. At the bottom of the image: the Arduino microprocessor, with the cable connecting it to the computer to update the code (during the experiments the Arduino was disconnected from the computer and connected to its wall mounted power supply). Above and to the left of the Arduino is the coil (inductor). Further up, the IGBT is shown with its the cooling fins. On the left side of the image is the side of the signal generator, behind it and to the right is the power supply unit used in the first experiments. The power supply unit used in these experiments is not shown in the figure. Also not shown in the figure- the Pearson coil and the CAA. The digital oscilloscope is in the top right corner.

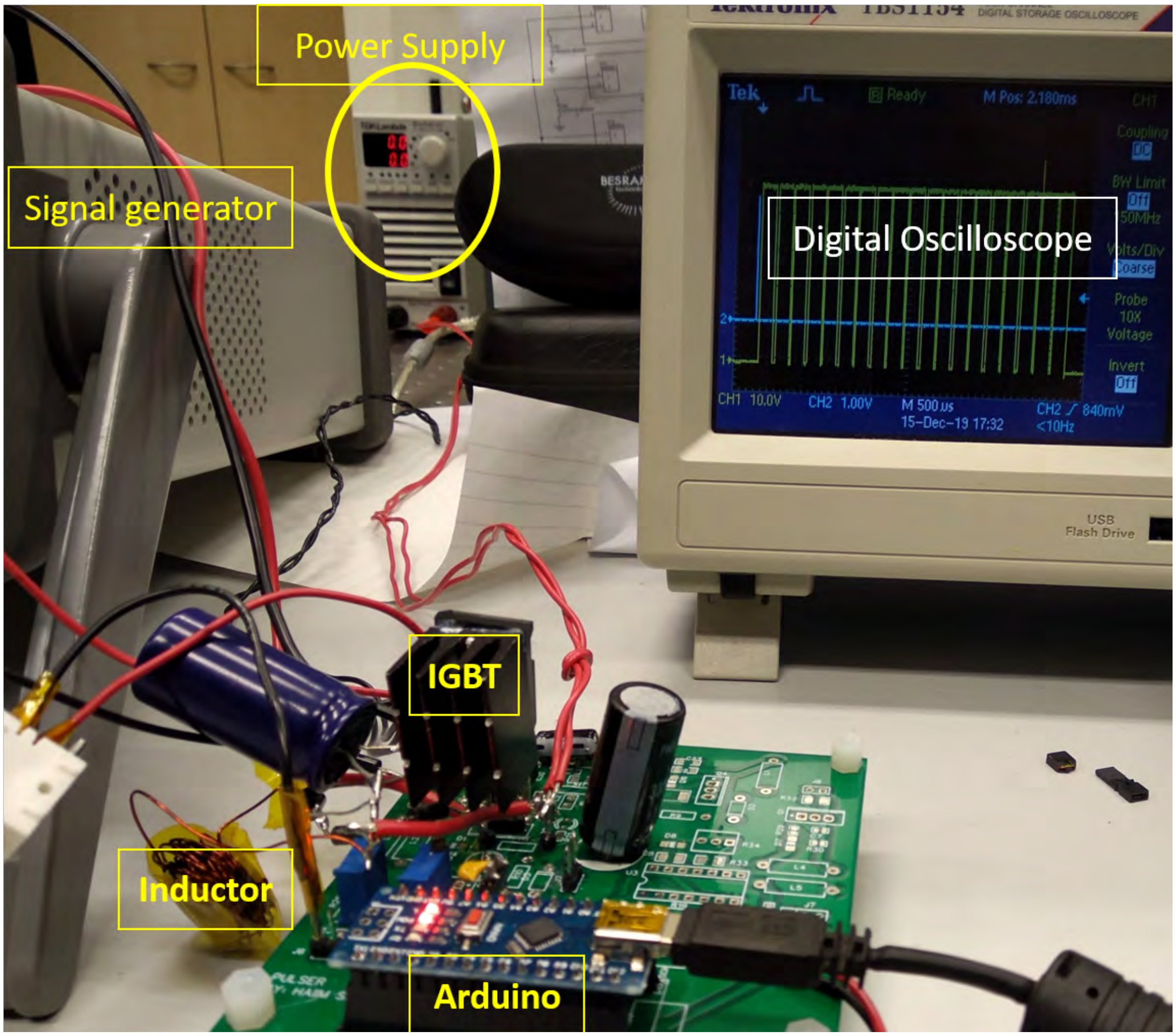

Figure 2.3: The experimental setup: Digital oscilloscope, signal generator, the PPU with IGBT, inductor and Arduino marked. The circled power supply unit is not the one used in the final experiments. Not pictured here: the CAA and the Pearson coil.

The inductance of the air coil was measured with an LC meter, it's initial value had been 24 μH. We removed 25 turns from the coil in order to allow the back voltage of the arc to reduce the inductor's current faster and terminate the arc faster then before. After this reduction the coil's inductance had been too small to measure, in the results section we estimate the new inductance value.

Another change in the system had been to the program controlling the PPU to better suit the scram-jet experiment conducted this semester.

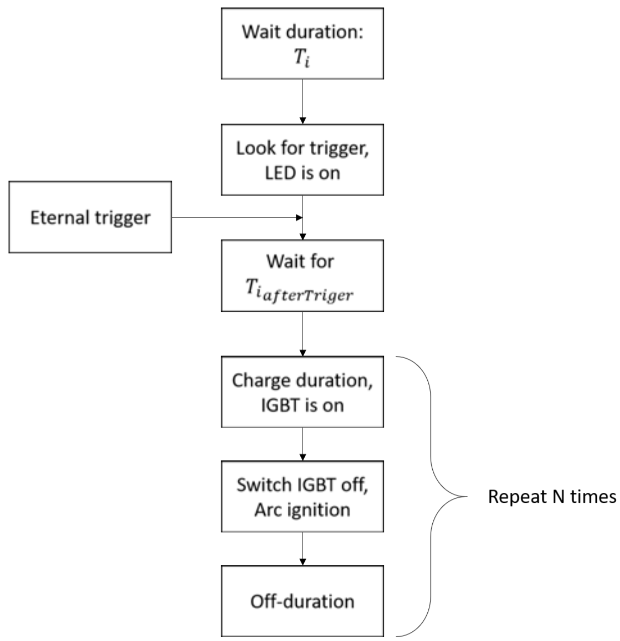

Figure 2.4: Program flow chart

T_i	Delay time before starting to look for trigger (ms)
$T_i afterTrig$	Delay time, after receiving external trigger, before starting the actuation process (ms)
N	Number of pulses in a test(#)
$ChargeTime$	Charging duration (t_{charge} μs), in which the IGBT is **on**
$targetCycle$	Targeted cycle time (μs), determined by required actuation frequency.
$offtimeWArc$	Time in which the IGBT is **off**,the arc ignites at the beginning of this stage and decays before it ends. This is determined according to the target cycle time.
PULSE_OUT_PIN	Indicates the output pin in the PPU's microprocessor that gets to the IGBT control.
Trig_in_PIN	The input pin through which the external trigger is received.

Table 2.3: Program parameters description

The program's flow chart is presented in Fig. 2.4, using the program parameters as described in table 2.3. As a safety measure, the controller does not start with actuation nor does it start by looking for its trigger, until after a waiting period. This had been required to avoid undesired actuation at startup. After the initial delay, the controller is in a loop that breaks once external trigger is detected in the specified input pin. To indicate that it is waiting for trigger, the LED is turned on (color- red). In the scram jet experiment, the trigger was connected to the camera recording the test. It had been required that the actuation would not start at the same time as the camera, thus an additional delay is added. Following the second delay, a "For loop" that counts the number of pulses generated is initiated. The number of pulses is chosen according to the actuation frequency, and the test duration. In each iteration of the loop, the IGBT is turned on for the set $ChargeTime$ duration to charge the coil. Then the IGBT is switched off, igniting the arc.

After the changes to the system, the discharge has a short, high peak and a tail that decays before the end of the cycle. After a cycle time the IGBT is turned on again in a new iteration.

The program is provided with explanatory comments in appendix A.

2.3 Results

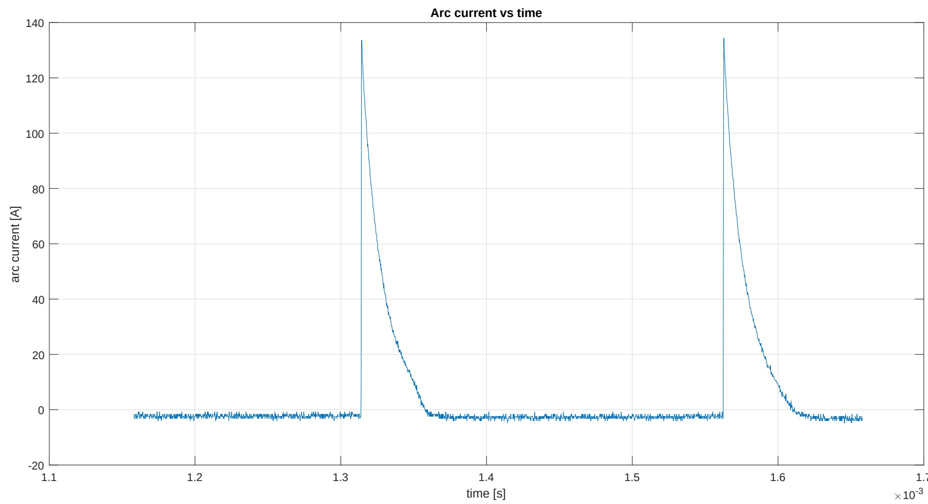

Figure 2.5: Measured discharge current vs. time, charging duration 50 μs. Supply voltage $V_{sup} = 42\ A$

Fig. 2.5 shows the current measured through the electrodes. The charging duration had been $t_{charge} = 50\ \mu s$, and from these measurements $I_{max} = 130\ A$ and $t_{arc} = 45\ \mu s$ (this is the time in which the current is not zero, for a single pulse). The width of half the pulse is $\sim 9\ \mu s$: a short, high peak and then a tail, as had been required.

Fig. 2.6 shows another measurement, in which the supply voltage was 30 V, the charging duration had been $t_{charge} = 50\ \mu s$, and from these measurements $I_{max} = 77\ A$ and $t_{arc} = 17\ \mu s$ (this is the time in which the current is not zero, for a single pulse). The width at half the amplitude is $\sim 8\ \mu s$, i.e. the pulse has a short, high peak and then a tail, as had been required.

2.3.1 Estimation of the New Inductance

Using the measurements with supply voltage of $V_{sup} = 30\ V$, such that only the coil is active (without contribution from the systems capacitor). We can calculate the energy in the coil and estimate the inductance.

$$\Delta t = 17\ \mu s, \quad V_{sup} = 30\ V, I_{max} = 77\ A$$

$$E_{coil} = \int_0^{\Delta t} I V_{sup} dt \approx \frac{1}{2} I_{max} V_{sup} \Delta t = 19.6\ mJ$$

$$E_{coil} = \frac{1}{2} L I_{max}^2$$

$$\Rightarrow \quad L \approx \frac{2E_{coil}}{I_{max}^2} = 6.6\ \mu H$$

2.4 Conclusions

The electrical setup of the CAA had been described along with the working principle. The changes to the system were documented as well as the resultant change in performance: shorter pulse width in high frequency.

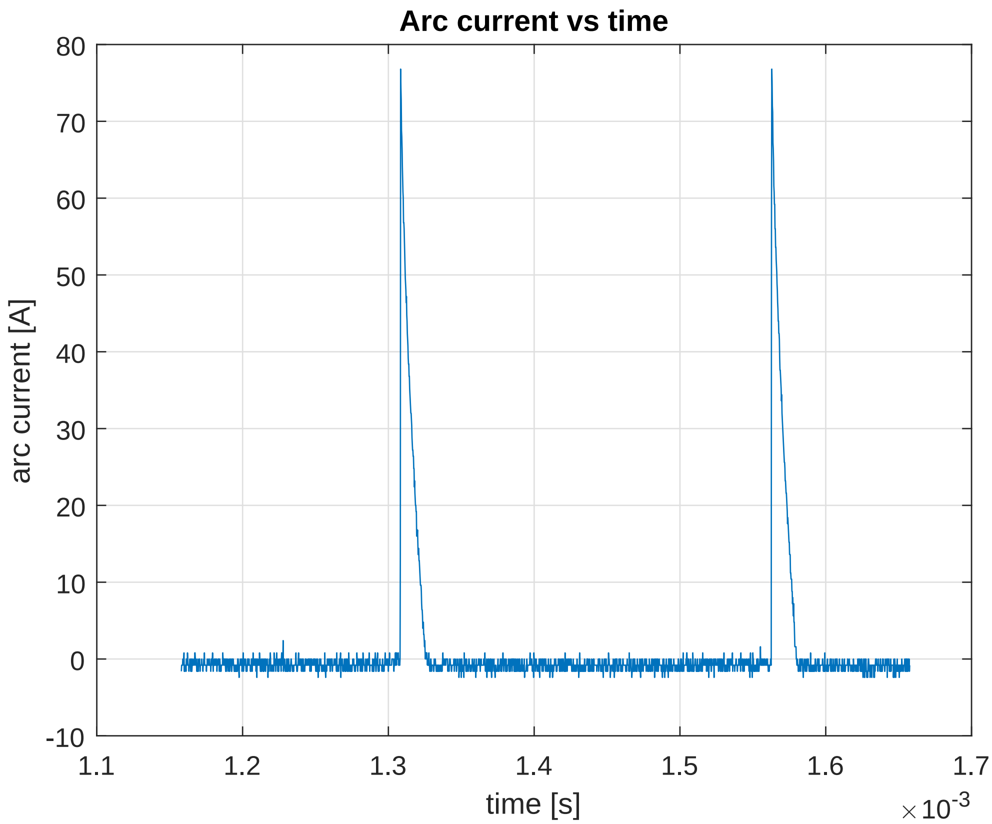

Figure 2.6: Measured discharge current vs. time, charging duration 50 μs. Supply voltage $V_{sup} = 30\ A$

Appendix A

Arduino Code

```
/* Arduino code for PPU, for operation in scramjet experiment
 * Other usful comments
 */
// Trigger related:
int Ti=1000;// [ms] wait some time (1sec) before begining to search for trigger
//int Ti_afterTrig=100;// [us] wait this much time after trigger before begining
operation
int Ti_afterTrig=10;// [ms] wait this much time after trigger before begining
operation
volatile int Operate = LOW; // This variable determines when to start operating
the actuator. the input from the trigger (volatile is used with interrupt since
this variable is about to change unexpectedly (i.e volatile))
// set pins:
const int PULSE_OUT_PIN = 9; // signal to switch, we connect this to the scope as
well
const int Trig_in_PIN = 11; // from this pin we recieve the trigger
// pulse numbers:
int N=40;  // total number of pulses in a run (not wanting to overheat the ppu),
not using packets.
// time settings:
int ChargeTime = 50;//[us]  *IGBT on*- coil charging, logical high?
int targetCycle_us=250;// [us] target cycle time-determins the frequency...
int offtimeWArc=targetCycle_us-ChargeTime; // IGBT is off, arc ignition and decay.
                  // the setup function runs once when you press reset or power
the board
void setup() {
  // set pins as either output or input:
  pinMode(13, OUTPUT); // set pin 13 (led) as an output, turns on when waiting
for trigger (steady light)
  pinMode(PULSE_OUT_PIN, OUTPUT); // set the signal pin as an output this
controls the switch
  pinMode(Trig_in_PIN, INPUT); // set trigger pin as input
  // write initial values to output pins:
  digitalWrite(PULSE_OUT_PIN, LOW);   // turn the signal on low, no charging, and
no plasma since there's no energy in the system yet
  digitalWrite(13, LOW);   // turn the LED off
}
                   // the loop function runs over and over again forever
void loop() {
                   // Pre-trigger:
delay(Ti); // wait a sec before start looking for trigger
// untill the trigger has been recieved, keep checking for it:
digitalWrite(13, HIGH);   // turn led on- lets us know it's looking for trigger
do {
 Operate=digitalRead(Trig_in_PIN); //read pin 11
} while (Operate== LOW); // only exit the while loop if got trigger
digitalWrite(13, LOW);   // turn the LED off- done looking
delayMicroseconds(Ti_afterTrig);// wait after trigger
                     // Post-trigger-
```

```
  for (int n= 0; n <(N-1); n++){
    // check if we passed the allowed number of pulses yet
    PORTB |= B00000010;//igbt is on, high
    delayMicroseconds(ChargeTime); //  charging coil
    PORTB &= B11111101;// igbt is off, low
    //delayMicroseconds(offtimeWArc);// for the rest of the cycle- the arc will
ignite and decay, the IGBT stays off
    delayMicroseconds(offtimeWArc);// for the rest of the cycle- the arc will
ignite and decay, the IGBT stays off
  }
}
/* Information that might be useful:
 * Arduino Nano pin configuration:
 *https://components101.com/microcontrollers/arduino-nano
 * How to avoid using delays
 *https://www.arduino.cc/en/Tutorial/BlinkWithoutDelay
 * Scope manual pdf
 *https://www.testequipmentdepot.com/tektronix/pdf/tbs1000_manual.pdf
 */
```

Appendix B

IGBT Data Sheet

Advance Technical Information

High Voltage IGBT

IXGH24N170
IXGT24N170

V_{CES} = 1700V
I_{C25} = 50A
$V_{CE(sat)} \leq$ 3.3V
$t_{fi(typ)}$ = 250ns

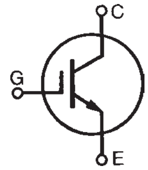

TO-247 (IXGH)

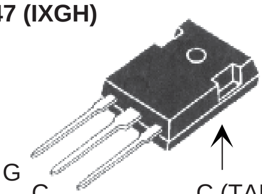

TO-268 (IXGT)

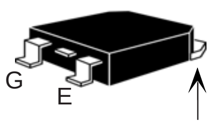

G = Gate　　C = Collector
E = Emitter　　TAB = Collector

Symbol	Test Conditions	Maximum Ratings	
V_{CES}	T_C = 25°C to 150°C	1700	V
V_{CGR}	T_J = 25°C to 150°C, R_{GE} = 1MΩ	1700	V
V_{GES}	Continuous	± 20	V
V_{GEM}	Transient	± 30	V
I_{C25}	T_C = 25°C	50	A
I_{C90}	T_C = 90°C	24	A
I_{CM}	T_C = 25°C, 1ms	150	A
SSOA	V_{GE} = 15V, T_{VJ} = 125°C, R_G = 5Ω	I_{CM} = 50	A
(RBSOA)	Clamped inductive load	@ 0.8 • V_{CES}	
t_{SC}	V_{GE} = 15V, T_{VJ} = 125°C, V_{CE} = 1000V	10	μs
(SCSOA)	R_G = 5Ω, non repetitive		
P_C	T_C = 25°C	250	W
T_J		-55 ... +150	°C
T_{JM}		150	°C
T_{stg}		-55 ... +150	°C
T_L	1.6mm (0.062 in.) from case for 10s	300	°C
T_{SOLD}	Plastic body for 10 seconds	260	°C
M_d	Mounting torque (TO-247)	1.13/10	Nm/lb.in.
Weight	TO-247	6	g
	TO-268	4	g

Symbol	Test Conditions (T_J = 25°C unless otherwise specified)		Characteristic Values Min.	Typ.	Max.	
BV_{CES}	I_C = 250μA, V_{GE} = 0V		1700			V
$V_{GE(th)}$	I_C = 250μA, V_{CE} = V_{GE}		3.0		5.0	V
I_{CES}	V_{CE} = 0.8 • V_{CES}				50	μA
	V_{GE} = 0V	T_J = 125°C			500	μA
I_{GES}	V_{CE} = 0V, V_{GE} = ± 20V				±100	nA
$V_{CE(sat)}$	I_C = I_{C90}, V_{GE} = 15V, Note 1			2.5	3.3	V
		T_J = 125°C		3.0		

Features

- International standard packages JEDEC TO-268 and JEDEC TO-247 AD
- High current handling capability
- MOS Gate turn-on
  - drive simplicity
- Rugged NPT structure
- Molding epoxies meet UL 94 V-0 flammability classification

Applications

- Capacitor discharge & pulser circuits
- AC motor speed control
- DC servo and robot drives
- DC choppers
- Uninterruptible power supplies (UPS)
- Switched-mode and resonant-mode power supplies

Advantages

- High power density
- Suitable for surface mounting
- Easy to mount with 1 screw, (isolated mounting screw hole)

Symbol	Test Conditions (T$_J$ = 25°C unless otherwise specified)	Characteristic Values Min.	Typ.	Max.	
g_{fs}	$I_C = I_{C90}$, V_{CE} = 10V, Note 1	18	25		S
$I_{C(ON)}$	V_{CE} = 10V, V_{GE} = 10V		100		A
C_{ies}	V_{CE} = 25V, V_{GE} = 0V, f = 1MHz		2400		pF
C_{oes}			120		pF
C_{res}			33		pF
Q_g	$I_C = I_{C90}$, V_{GE} = 15V, V_{CE} = 0.5 • V_{CES}		106		nC
Q_{ge}			18		nC
Q_{gc}			32		nC
$t_{d(on)}$	**Inductive load, T$_J$ = 25°C**		42		ns
t_{ri}	$I_C = I_{C25}$, V_{GE} = 15V		39		ns
$t_{d(off)}$	V_{CE} = 0.8 • V_{CES}, $R_G = R_{off}$ = 5Ω		200	400	ns
t_{fi}	Remarks: Switching times may increase for V_{CE} (Clamp) > 0.8 • V_{CES},		250	500	ns
E_{off}	higher T_J or increased R_G		8	12	mJ
$t_{d(on)}$	**Inductive load, T$_J$ = 125°C**		50		ns
t_{ri}	$I_C = I_{C25}$, V_{GE} = 15V		55		ns
E_{on}	V_{CE} = 0.8 • V_{CES}, $R_G = R_{off}$ = 5Ω		2.0		mJ
$t_{d(off)}$	Remarks: Switching times may		200		ns
t_{fi}	increase for V_{CE} (Clamp) > 0.8 • V_{CES},		360		ns
E_{off}	higher T_J or increased R_G		12		mJ
R_{thJC}				0.50	°C/W
R_{thCS}	(TO-247)		0.25		°C/W

Note 1: Pulse test, t ≤ 300μs, duty cycle, d ≤ 2%.

Min Recommended Footprint

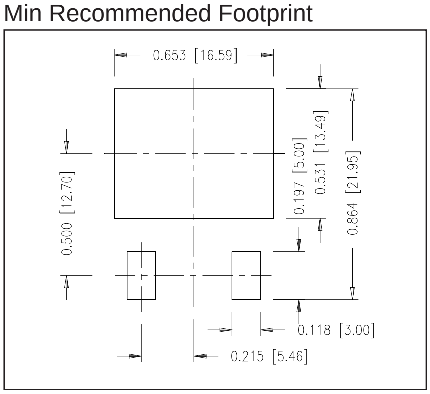

TO-247 AD Outline

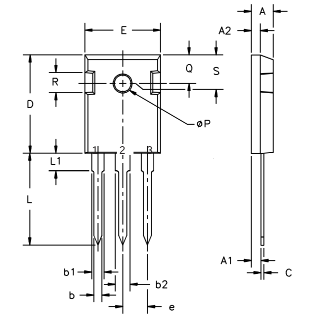

Terminals: 1 - Gate 2 - Drain

Dim.	Millimeter Min.	Max.	Inches Min.	Max.
A	4.7	5.3	.185	.209
A_1	2.2	2.54	.087	.102
A_2	2.2	2.6	.059	.098
b	1.0	1.4	.040	.055
b_1	1.65	2.13	.065	.084
b_2	2.87	3.12	.113	.123
C	.4	.8	.016	.031
D	20.80	21.46	.819	.845
E	15.75	16.26	.610	.640
e	5.20	5.72	0.205	0.225
L	19.81	20.32	.780	.800
L1		4.50		.177
∅P	3.55	3.65	.140	.144
Q	5.89	6.40	0.232	0.252
R	4.32	5.49	.170	.216

TO-268 Outline

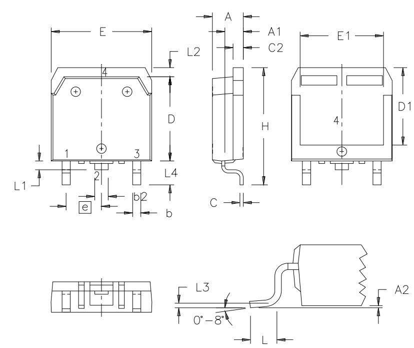

Terminals: 1 - Gate 2 - Drain

SYM	INCHES MIN	MAX	MILLIMETERS MIN	MAX
A	.193	.201	4.90	5.10
A1	.106	.114	2.70	2.90
A2	.001	.010	0.02	0.25
b	.045	.057	1.15	1.45
b2	.075	.083	1.90	2.10
C	.016	.026	0.40	0.65
C2	.057	.063	1.45	1.60
D	.543	.551	13.80	14.00
D1	.488	.500	12.40	12.70
E	.624	.632	15.85	16.05
E1	.524	.535	13.30	13.60
e	.215 BSC		5.45 BSC	
H	.736	.752	18.70	19.10
L	.094	.106	2.40	2.70
L1	.047	.055	1.20	1.40
L2	.039	.045	1.00	1.15
L3	.010 BSC		0.25 BSC	
L4	.150	.161	3.80	4.10

ADVANCE TECHNICAL INFORMATION

The product presented herein is under development. The Technical Specifications offered are derived from a subjective evaluation of the design, based upon prior knowledge and experience, and constitute a "considered reflection" of the anticipated result. IXYS reserves the right to change limits, test conditions, and dimensions without notice.

Appendix C

Arduino Nano Schematics

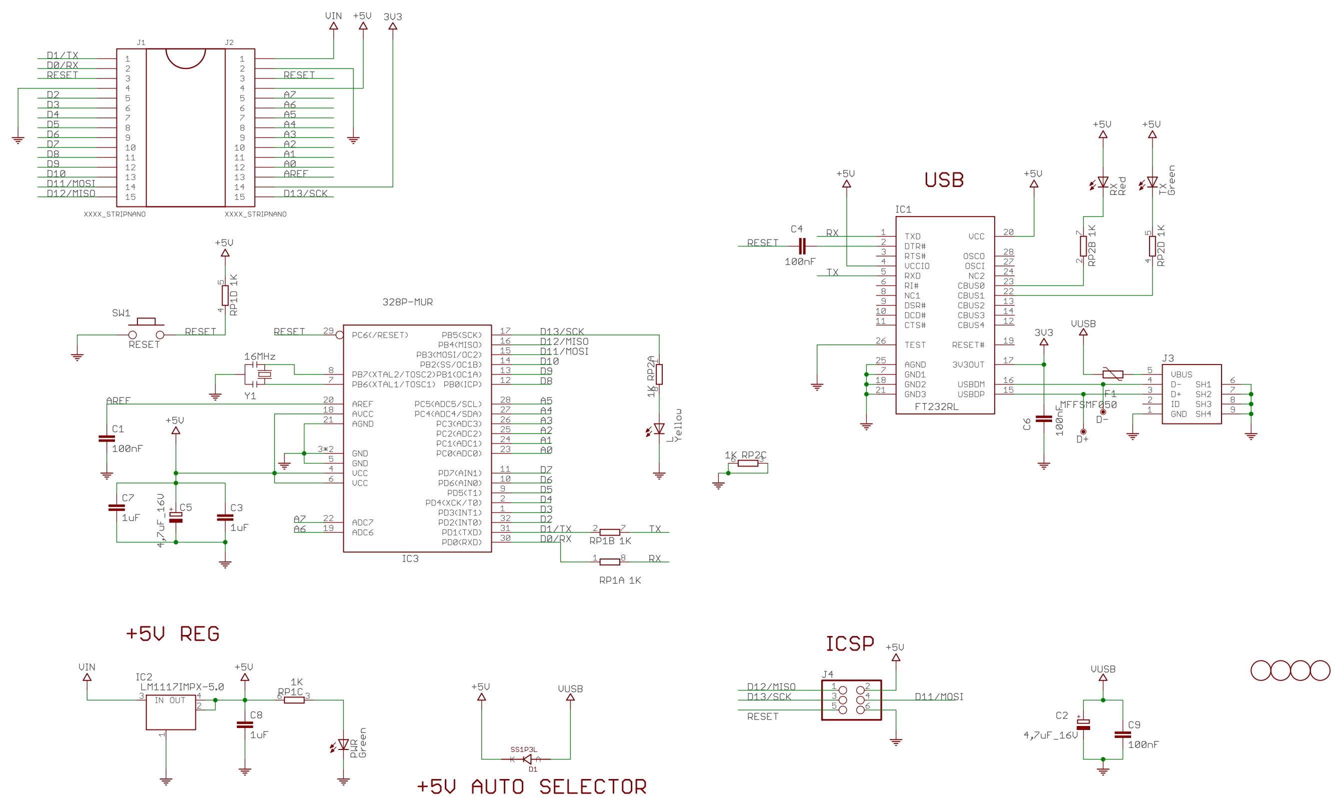

Arturo Guadalupi

NanoV3.3

23/01/19 15:50

Sheet: 1/1

Bibliography

[1] Igbt data sheet. https://www.digikey.com/product-detail/en/ixys/IXGH24N170/IXGH24N170-ND/1652160.

[2] Testing methodology for quantifying the influence of plasma actuator on subsonic flow separation. https://aerospace.technion.ac.il/studies/ug-studies/student-research-projects/.

[3] Matar M. Rosen, Anton Ronis, and Igal Kronhaus. The influence of cathodic arc jet on separated subsonic flow over backward facing step. Will be published at sumepoint, 2020 – *Submitted*.

[4] David Greenblatt and Israel J. Wygnanski. The control of flow separation by periodic excitation. Progress in Aerospace Sciences, 36(7):487 – 545, 2000.

[5] Avi Seifert, David Greenblatt, and Israel J. Wygnanski. Active separation control: an overview of reynolds and mach numbers effects. Aerospace Science and Technology, 8(7):569 – 582, 2004.

[6] D Dolgopyat and A Seifert. Active flow control virtual maneuvering system applied to conventional airfoil. AIAA Journal, 57(1):72–89, 2018.

[7] A Seifert, S Eliahu, D Greenblatt, and I Wygnanski. Use of piezoelectric actuators for airfoil separation control. AIAA journal, 36(8):1535–1537, 1998.

[8] Eric Moreau. Airflow control by non-thermal plasma actuators. Journal of physics D: applied physics, 40(3):605, 2007.

[9] Yurii G Utkin, Saurabh Keshav, Jin-Hwa Kim, Jeff Kastner, Igor V Adamovich, and Mo Samimy. Development and use of localized arc filament plasma actuators for high-speed flow control. Journal of Physics D: Applied Physics, 40(3):685, 2006.

[10] M Samimy, I Adamovich, B Webb, J Kastner, J Hileman, S Keshav, and P Palm. Development and characterization of plasma actuators for high-speed jet control. Experiments in Fluids, 37(4):577–588, 2004.

[11] Anton Ronis and Igal Kronhaus. Spatial spectroscopic analysis of a cathodic arc jet. In AIAA Scitech 2019 Forum, page 0738, 2019.

[12] Anton Ronis and Igal Kronhaus. Thrust generation of the cathodic arc in ambient air. Journal of Physics D: Applied Physics, 52(32):324004, jun 2019.

[13] Anton Ronis. Experimental characterization of the cathodic arc actuator for flow manipulation (doctoral dissertation).